Supplementary Materials for “Axion Topology in Photonic Crystal Domain Walls”

Chiara Devescovi*,[1,*] Antonio Morales-Pérez*,[1,†] Yoonseok Hwang,[2] Mikel García-Díez,[1,3] Iñigo Robredo,[4,1] Barry Bradlyn,[2] Juan Luis Mañes,[3] Aitzol García-Etxarri,[1,5,‡] and Maia G. Vergniory[4,1,§]

[1]*Donostia International Physics Center, Paseo Manuel de Lardizabal 4, 20018 Donostia-San Sebastian, Spain.*
[2]*Department of Physics, University of Illinois at Urbana-Champaign, Urbana, IL, USA*
[3]*Physics Department, University of the Basque Country (UPV/EHU), Bilbao, Spain*
[4]*Max Planck Institute for Chemical Physics of Solids, Dresden D-01187, Germany*
[5]*IKERBASQUE, Basque Foundation for Science, María Díaz de Haro 3, 48013 Bilbao, Spain.*

(Dated: August 18, 2023)

1. MAGNETIC SPACE GROUP ANALYSIS

In this section, we analyze the Magnetic Space Group (MSG) for the gyrotropic Photonic Crystals (PhCs). The MSG assignation is conducted on the dielectric structure, via the use of the FINDSYM software [1]. We perform this analysis for the case of a Supercell Modulation (SM) of a $N = 3$ period, with phase $\phi = 0, \pi$ and in presence of an external magnetic field :

$$\mathbf{H} = (|h|\cos(\sigma), |h|\sin(\sigma), H_z) \tag{S1}$$

with $|h| << |H_z|$. We evaluate the symmetry content of the electromagnetic fields, via the study of the transformation properties of the $\mathbf{D}$ electric and $\mathbf{B}$ magnetic modes supported by the PhC, using the MPB solver [2], as explained in the Method section.

We label the irreducible representations (irreps) at the high-symmetry points (HSPs) according to the notation of Bilbao Crystallographic Server (BCS) [3, 4]. We compute the symmetry vector $\tilde{\mathbf{v}}$, which contains the multiplicity of each irrep in the little group of each HSP. From these, we finally extract the corresponding Symmetry Indicators (SI) [5–10]. Please note that all operations and coordinates are expressed with respect to the following primitive lattice vectors:

$$\mathbf{e}_1 = \hat{\mathbf{x}}, \quad \mathbf{e}_2 = \hat{\mathbf{y}}, \quad \mathbf{e}_3 = 3\hat{\mathbf{z}}. \tag{S2}$$

These lattice vectors are those of the BCS parent Space Group (SG) #224. We will stick to this cartesian system even for the lower symmetry phases.

Case with $|h| = 0$

When the gyrotropic axis is along z, i.e. in presence of an external $\mathbf{H} = (0, 0, H_z)$ magnetic field, the PhCs are in MSG 67.505. Please note that there is a $\pi/4$ rotation in the OXY plane between SG 224 and MSG 67.505.

To label the irreps at the HSP, we consider the maximal unitary subgroup of MSG #67.505 (Cm'm'a), i.e. Space Group (SG) #13 ($P2/m$), whose generators are:

$$\{C_{2z}|\frac{1}{2}, \frac{1}{2}, 0\}, \quad \{m_z|\frac{1}{2}, \frac{1}{2}, 0\}, \quad \{\bar{1}|0, 0, 0\}, \tag{S3}$$

expressed in the basis of Eq. S2. The anti-unitary generators of MSG #67.505 are:

$$\begin{aligned} &\{C'_{2_{110}}|\frac{1}{2}, \frac{1}{2}, 0\}, \quad \{m'_{110}|\frac{1}{2}, \frac{1}{2}, 0\}, \\ &\{C'_{2_{1\bar{1}0}}|0, 0, 0\}, \quad \{m'_{1\bar{1}0}|0, 0, 0\}, \end{aligned} \tag{S4}$$

which are also expressed in the basis of Eq. S2 and where the prime indicates the time-reversal operation. Please note that there is a $\pi/2$ rotation in the OYZ plane between MSG 67.505 and SG 13.

The symmetry vectors, computed for the lowest six transverse bands of the PhC are:

$$\begin{aligned} \tilde{\mathbf{v}}^T_{\phi=0} = [&3A_1, 3B_1, C_1^- + 2C_2^+ + 3C_2^-, 3D_1, 3E_1, (\blacksquare)^{2T} \\ &+ 2\Gamma_2^+ + 2\Gamma_2^-, Y_1^- + 2Y_2^+ + 3Y_2^-, 3Z_2^+ + 3Z_2^-] \end{aligned} \tag{S5}$$

and

$$\begin{aligned} \tilde{\mathbf{v}}^T_{\phi=\pi} = [&3A_1, 3B_1, C_1^- + 2C_2^+ + 3C_2^-, 3D_1, 3E_1, (\blacksquare)^{2T} \\ &+ 2\Gamma_2^+ + 2\Gamma_2^-, Y_1^+ + 3Y_2^+ + 2Y_2^-, 3Z_2^+ + 3Z_2^-] \end{aligned} \tag{S6}$$

where $(\blacksquare)^{2T}$ indicates the irregular symmetry content at Γ and $\omega = 0$ arising from transversality of the electromagnetic waves [11, 12], where $()^T$ labels the transverse bands and where ˜ superscript indicates that the analysis is done after the introduction of the SM.

Note that HSPs labeled as Y, Z, C correspond to the following reduced coordinates in the Brillouin Zone (BZ), whose little group has solely 1-dimensional irreps:

$$Y = (\pi, \pi, 0), \quad Z = (0, 0, \pi), \quad C = (\pi, \pi, \pi). \tag{S7}$$

The HSPs A, B, D, E, whose little group has a single 2-dimensional irrep, correspond to the following:

$$A = (\pi, 0, 0), \quad B = (0, \pi, 0), \quad D = (0, \pi, \pi), \quad E = (\pi, 0, \pi). \tag{S8}$$

On the other hand, for the lowest modes of the Tranversality-Enforced Tight-Bindind (TETB) model, we obtain:

$$\begin{aligned} \tilde{\mathbf{v}}^{T+L}_{\phi=0} = [&6A_1, 6B_1, 3C_1^+ + 4C_1^- + 2C_2^+ + 3C_2^-, 6D_1, \\ &6E_1, 2\Gamma_1^+ + 4\Gamma_1^- + 2\Gamma_2^+ + 4\Gamma_2^-, 3Y_1^+ + 4Y_1^- \\ &+ 2Y_2^+ + 3Y_2^-, 3Z_1^+ + 3Z_1^- + 3Z_2^+ + 3Z_2^-] \end{aligned} \tag{S9}$$

and

$$\tilde{\mathbf{v}}^{T+L}_{\phi=\pi} = [6A_1, 6B_1, 3C_1^+ + 4C_1^- + 2C_2^+ + 3C_2^-, 6D_1, 6E_1, 2\Gamma_1^+ + 4\Gamma_1^- + 2\Gamma_2^+ + 4\Gamma_2^-, 4Y_1^+ + 3Y_1^- + 3Y_2^+ + 2Y_2^-, 3Z_1^+ + 3Z_1^- + 3Z_2^+ + 3Z_2^-]. \tag{S10}$$

These equations are in correspondence with Eqs. M6-M9 of the main text, where we take into account solely inversion symmetry.

After having identified the irregular irrep content at Γ, as $(\blacksquare)^{2T} = -\Gamma_1^+ + \Gamma_1^- + 2\Gamma_2^-$, consistent with symmetry-constrained decomposition for point group $2/m$ as in Refs. [11, 12], we can split the TETB symmetry vector as follows: $\tilde{\mathbf{v}}^{T+L}_{\phi} = \tilde{\mathbf{v}}^{T}_{\phi} + \tilde{\mathbf{v}}^{L}_{\phi}$.

Since $\tilde{\mathbf{v}}^{L}_{\phi}$ have trivial SI, we can extract the transverse SI for the photonic bands obtaining:

$$\begin{aligned} \nu^{T+L}_{\phi=0} &= \{1, 0\} \\ \nu^{T+L}_{\phi=\pi} &= \{1, 1\} \end{aligned} \tag{S11}$$

corresponding to the $\mathbb{Z}_2 \times \mathbb{Z}_2$ magnetic SI group, see Table 5 in Ref. [5].

Case with $|h| << |H_z|$

When we apply a small off-z tilt to the external magnetic field, as described by Eq. S1, the PhC undergoes subduction to MSG #2.4 ($P\bar{1}$). As long as the $|h|$ perturbation is weak enough as compared to $|H_z|$, the transition occurs without closing the bulk Chern gap, leaving the Chern numbers unaffected, with

$$(C_x, C_y, C_z) = (0, 0, 1). \tag{S12}$$

More precisely, the $|h|$ component introduces a small deviation from the Weyl folding commensurate condition, which results in a gradual shrinking of the bulk 3D Chern gap as $|h|$ is increased. However, as long as the bulk 3D Chern gap remains opens and Eq. S12 condition is satisfied, the SI analysis done for $|h| = 0$ uniquely determines the SIs for the $|h| \neq 0$ case. The reason for this is that the SI group for MSG #2.4, which is $\mathbb{Z}_2^3 \times \mathbb{Z}_4$, is a supergroup of $\mathbb{Z}_2^2$ in MSG #67.505. Applying the compatibility relations in MSG #67.505 to the well-know expression for the inversion SI [5–10], returns that $\{\bar{z}_{2,x}, \bar{z}_{2,y}, \bar{z}_{2,z}|\bar{z}_4\}$ can only takes value in:

$$\{0, 0, 0|0\}, \quad \{0, 0, 0|2\}, \quad \{0, 0, 1|0\}, \quad \{0, 0, 1|2\}, \tag{S13}$$

thus forming $\mathbb{Z}_2^2$. The transverse SI for the photonic bands in presence of $0 < |h| << |H_z|$, computed in the MSG 2.4 setting, are:

$$\begin{aligned} \nu^{T+L}_{\phi=0} &= \{0, 0, 1|0\} \\ \nu^{T+L}_{\phi=\pi} &= \{0, 0, 1|2\} \end{aligned} \tag{S14}$$

which is in agreement with Eq. S11, which were obtained in SG 13 setting. In SG 13, the $\mathcal{I}$-SI $\{\bar{z}_{2,x}, \bar{z}_{2,y}, \bar{z}_{2,z}|\bar{z}_4\}$ are reduced to

$$\bar{z}_{2,x} = \bar{z}_{2,y} = 0 \mod 2 \tag{15}$$

$$\bar{z}_{2,z} = n(\Gamma_1^-) + n(\Gamma_2^-) + n(Y_1^-) + n(Y_2^-) \mod 2 \tag{16}$$

$$\bar{z}_4 = 2n(\Gamma_2^-) + 2n(Y_2^-) + 2n(C_1^-) + 2n(Z_1^-) \mod 4 \tag{17}$$

where $n(irrep)$ counts the irrep multiplicity at the corresponding HSP. There relations directly follow from applying compatibility constraints. Importantly, note that $\bar{z}_4 \in \{0, 2\}$. This shows that the *relative* Axion Insulators (rAXI) with $\phi = 0, \pi$ display an obstruction of their $\bar{z}_4$ symmetry indicators, irrespective of the presence of a small $|h|$ magnetic perturbation.

2. BOUNDARY CONDITION FOR THE DOMAIN-WALL

In the main text, we construct phase-obstructed domain walls of PhCs, with the $\phi(x)$ SM phase changing from $\phi(x) = 0$ for $x < 0$, to $\phi(x) = \pi$ for $x > 0$. Even in the presence of the domain wall, the AXI PhC is a continuous and fully connected structure, with the rods connected all across the interface. The electromagnetic modes supported by the PhC can be numerically simulated by solving the Maxwell's equations on a dense real-space grid, where discontinuities in the dielectric constant are treated via a simple linear interpolation on a dense mesh. Specifically, we use the MIT Photonic-Bands package (MPB) [2] in this case. Conversely, TB models are typically constructed using discrete orbitals localized at specific Wyckoff positions. To accurately capture the continuous nature of PhC geometry in the TETB model, we employ a specific boundary condition choice:

- We keep the hopping terms constant across the interface;
- We use a linear interpolation to transition between the onsite energies of the subsystems with SM $\phi = 0$ and $\phi = \pi$.

This prevents the emergence of surface effects in the TETB which deviate from the surface electromagnetic response of a fully connected 3D photonic structure. Specifically, for the model considered here, this boundary choice ensures that the SM mass term which couples the Weyl points [13]:

$$m = \Delta e^{i\phi}, \tag{S18}$$

crosses zero across a domain wall where $m(x \to -\infty) = m$ and $m(x \to \infty) = -m$, where (Δ, ϕ) are amplitude and phase of the SM. This ensures the domain wall bands are gapless at criticality, as shown in Fig. S1(a).

3. GAPLESS DIRAC CONE ON THE $x = 0$ PLANE

As shown in Fig. S1(a), the $\delta\theta = \pi$ domain wall bands display a massless 2D Dirac cone, located at $(k_y, k_z) = (\pi, \pi)$ in the surface BZ. This gapless state arises as a projection of the folded bulk Weyl points $V = (\pi, \pi, 0)$, when $\delta\theta = \pi$, and when the external magnetic field complies with the commensuration folding condition and does not present any component orthogonal to the interface plane. More specifically, since

$$m(x = 0) = 0, \tag{S19}$$

the nested Weyl points reappear as a projection of the bulk Weyl points on the $x = 0$ plane, due to the local cancellation of the effects of the SM. At $x = 0$, the rAXI irreps are exchanged through the phase-obstructed domain wall as a result of the double band inversion occurring in the bulk at V, which is the point where folding of the Weyl points occurs. Importantly, this Dirac cone is not robust to perturbations at the boundary. In particular, the gapless condition for the surface modes on the $x = 0$ plane is only maintained as long as the magnetic field does not present any component orthogonal to the interface, i.e., for an x-domain wall, when

$$h_x = |h|\cos(\sigma) = 0. \tag{S20}$$

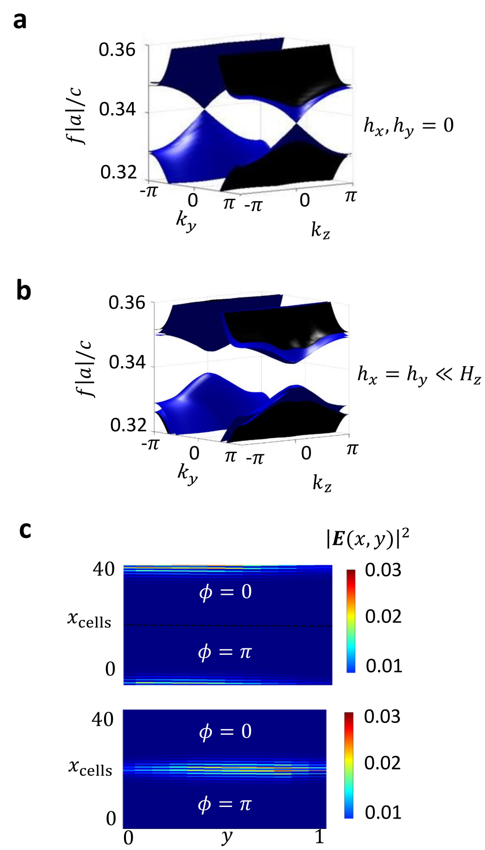

FIG. S1. Surface bands for a x domain wall with $\delta\phi = \delta\theta = \pi$. Gapless configuration in panel (a), gapped configuration in panel (b), in presence of a small magnetic perturbation $|h|$ in the xy plane. Localization of the surface modes at the interface in panel (c). Projected bulk bands in black, surface bands in blue.

4. MAGNETIC CONTROL OF THE SURFACE GAP

To impart a mass to the Dirac cone, we introduce a small magnetic perturbation in the xy plane with $|h| << |H_z|$, resulting in the gapped domain wall bands displayed in Fig. S1(b). As shown in Fig. S2, by tuning the value of $|h|$ it is possible to control the size of this surface gap. For example, for a fixed value of $\sigma = \pi/4$, the optimum gap is reached at $|h| \sim 1$. Note that $|h|$ has to be treated as a perturbation as compared to H_z: for values of $|h| \sim |H_z|$, the gap tends to close again, due to deviation from the Weyl folding condition, and correspondent shrinking of the bulk gap.

4. TOPOLOGICAL TRANSITION BETWEEN DIFFERENT SURFACE HINGE CONFIGURATIONS

In the main text, we verified that it is possible to induce topological transitions across different hinge-state configurations by tuning the σ angle and rotating magnetic perturbation in the xy plane. This results in four distinct hinge-state configurations α,β,γ,δ, with localization of the upwards moving state on either of the four different hinges. Since these transitions occur across these topologically-distinct boundary configurations, we expect them to be accompanied by a gap closing point. Indeed, as shows in Fig. S3, for a x domain wall, the gap closes when the magnetic perturbation is along $\pm y$. We checked that the same happens for a y domain wall, with a gap closing when the magnetic perturbation is along 10, i.e. $\pm x$. These four values of the in-plane angle:

$$\sigma = 0, \frac{\pi}{2}, \pi, \frac{3\pi}{2} \tag{S21}$$

correspond to magnetic orientations which do not break any symmetry among the four inversion-symmetric hinge-configurations.

5. RELATIVE PHASE DIFFERENCE

As already observed, an x domain wall across phase obstructed 3D Chern photonic insulators, behaves as the critical point between AXI and a trivial insulator, as long

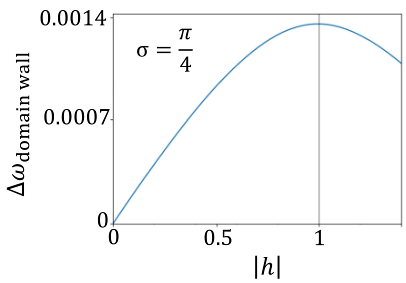

FIG. S2. Dependence of the surface gap with respect to the amplitude of the magnetic perturbation $|h|$, for an x domain wall and for a fixed angle $\sigma = \pi/4$, as computed for the TETB model.

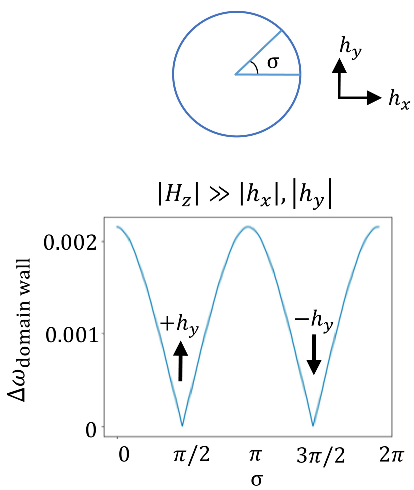

FIG. S3. Dependence of the surface gap with respect to the σ in-plane angle of the magnetic perturbation, for an x domain wall and for a fixed amplitude $|h| = 1$, as computed for the TETB model.

as the SM phase satisfies $\delta\phi = \delta\theta = \pi$. Fig. S4 shows the surface bands while deviating from this condition, setting

$$-\pi < \delta\theta < \pi. \tag{S22}$$

As depicted, the surface bands gradually disappear as the phase difference is tuned to 0, recovering the projected 3D Chern gap. The surface modes then reappear as the sign of the phase difference is reversed, reaching criticality again when $\delta\theta = -\pi = \pi \pmod{2\pi}$.

* chiara.devescovi@dipc.org
† antonio.morales@dipc.org
‡ aitzolgarcia@dipc.org
§ maia.vergniory@cpfs.mpg.de

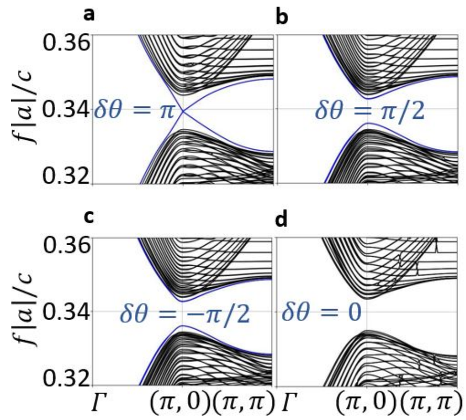

FIG. S4. Dependence of the surface gap for an x domain wall with respect to the value of the $\delta\phi = \delta\theta$ phase difference across the interface. Projected bulk bands in black, surface bands in blue.

[1] Harold T Stokes and Dorian M Hatch. Findsym: program for identifying the space-group symmetry of a crystal. *Journal of Applied Crystallography*, 38(1):237–238, 2005.

[2] Steven G Johnson and John D Joannopoulos. Block-iterative frequency-domain methods for maxwell's equations in a planewave basis. *Optics express*, 8(3):173–190, 2001.

[3] Mois I Aroyo, Juan Manuel Perez-Mato, Danel Orobengoa, EMRE Tasci, Gemma de la Flor, and Asel Kirov. Crystallography online: Bilbao crystallographic server. *Bulg. Chem. Commun*, 43(2):183–197, 2011.

[4] Luis Elcoro, Barry Bradlyn, Zhijun Wang, Maia G Vergniory, Jennifer Cano, Claudia Felser, B Andrei Bernevig, Danel Orobengoa, G Flor, and Mois I Aroyo. Double crystallographic groups and their representations on the bilbao crystallographic server. *Journal of Applied Crystallography*, 50(5):1457–1477, 2017.

[5] Haruki Watanabe, Hoi Chun Po, and Ashvin Vishwanath. Structure and topology of band structures in the 1651 magnetic space groups. *Science advances*, 4(8):eaat8685, 2018.

[6] Heejae Kim, Ken Shiozaki, and Shuichi Murakami. Glide-symmetric magnetic topological crystalline insulators with inversion symmetry. *Physical Review B*, 100(16):165202, 2019.

[7] Ryo Takahashi, Yutaro Tanaka, and Shuichi Murakami. Bulk-edge and bulk-hinge correspondence in inversion-symmetric insulators. *Physical Review Research*, 2(1):013300, 2020.

[8] Yuanfeng Xu, Luis Elcoro, Zhi-Da Song, Benjamin J Wieder, MG Vergniory, Nicolas Regnault, Yulin Chen, Claudia Felser, and B Andrei Bernevig. High-throughput calculations of magnetic topological materials. *Nature*, 586(7831):702–707, 2020.

[9] Luis Elcoro, Benjamin J Wieder, Zhida Song, Yuanfeng Xu, Barry Bradlyn, and B Andrei Bernevig. Magnetic topological quantum chemistry. *Nature communications*, 12(1):1–10, 2021.

[10] Hoi Chun Po. Symmetry indicators of band topology. *Journal of Physics: Condensed Matter*, 32(26):263001,

2020.

[11] Thomas Christensen, Hoi Chun Po, John D Joannopoulos, and Marin Soljačić. Location and topology of the fundamental gap in photonic crystals. *Physical Review X*, 12(2):021066, 2022.

[12] Antonio Morales Perez, Chiara Devescovi, Yoonseok Hwang, Mikel Garcia Diez, Barry Bradlyn, Juan Luis Manes, Maia Garcia Vergniory, and Aitzol Garcia Etxarri. Transversality-enforced tight-binding model for 3d photonic crystals aided by topological quantum chemistry. *arXiv:2305.18257*.

[13] Dan Sehayek, Manisha Thakurathi, and AA Burkov. Charge density waves in weyl semimetals. *Physical Review B*, 102(11):115159, 2020.